Advances in Aerodynamics

RESEARCH Open Access

On the effects of non-zero yaw on leading-edge tubercled wings

T. H. New[1*] and S. Mandrà[2]

*Correspondence:
dthnew@ntu.edu.sg

[1] School of Mechanical and Aerospace Engineering, Nanyang Technological University, 50 Nanyang Avenue, Singapore 639798, Singapore
[2] Institut für Fluiddynamik, ETH Zürich, Sonneggstrasse 3, Zürich 8092, Switzerland

Abstract

Steady-state numerical simulations were conducted to capture the aerodynamic characteristics and flow patterns resulting from a tubercled and non-tubercled wing subjected to various combined pitch and yaw conditions at $Re = 1.8 \times 10^5$. Pitch angle ranged from 0° to 25°, while two different yaw angles of 10° and 30° were used. Results show that 10° yaw angle does not impact upon the lift and drag characteristics significantly, while a 30° yaw angle leads to substantial lift and drag losses. Additionally, the tubercled wing continues to confer favourable stall-mitigating characteristics even for the larger yaw angle. Finally, despite skewing the flow structures significantly, the 30° yaw angle also reduces the formations of bi-periodic flow structures, flow separations and recirculating regions along the leading-edge tubercles, suggesting potentially better flow stability and controllability.

Highlights

- Steady-state numerical study is conducted on NACA 634021 baseline and tubercled wings
- Two yaw angles of 10° and 30° are used together with pitch angles from 0° to 25°
- Results show 10° yaw angle has minimal impact on the lift and drag characteristics, while 30° yaw angle reduces both lift and drag levels significantly
- Larger yaw angle leads to more skewed flows, as well as reduced flow separations and recirculating regions
- Larger yaw angle also suppresses bi-periodic flow behaviour in tubercled wings, suggesting better flow stability and controllability

Keywords: Leading-edge tubercles, Finite wings, Vortex systems, Yaw, Numerical simulation

1 Introduction

Modifications to conventional lifting surfaces have often been seen as a simple but robust approach to improve their flow control and aerodynamic performances, particularly in terms of their lift, drag or aeroacoustics behaviour. This is especially the case for passive flow control modifications where recent investigations have reaffirmed their promising outcomes when it comes down to stall-delay [1–4], lift enhancements [5, 6], drag [7, 8] and aeroacoustics signature reductions [9–11]. At the same time, bio-inspired solutions

based on sinusoidal tubercles along the leading-edges of lifting surfaces have also gained much popularity. Extensive studies involving the use of regularly distributed leading-edge tubercles or protuberances on aerial/marine vehicle lifting surfaces [12–22], fins or rudders [23, 24], propeller blades [25–27], compressor and turbine blades [28–30], among others, have been conducted since the seminal work [31] on the hydrodynamic design and functions of humpback whale flippers. For a more extensive coverage and review of earlier work carried out on this topic, readers are referred to [32] for further details. The general consensus among various researchers is that leading-edge tubercles exert favourable flow influences by producing coherent streamwise vortices that could mitigate severe flow separations, which in turn leads to stall delay or even prevention. On the other hand, the presence of dynamic stall and flow hysteresis under some conditions means that there remain limits to how wide the operating range of leading-edge tubercles could be extended, and that fine-tuning the tubercle wavelength and amplitude is a key consideration during the design process.

Despite the extensive amount of work conducted on tubercled wings designed to improve aerodynamic or hydrodynamic performance of lifting surfaces, most studies focused on non-swept wings encountering free streams perpendicularly. As for the small number of studies that made use of swept wings, a non-perpendicular free stream direction is incident rather than a dedicated effort specifically made to understand the impact of aircraft under side-slip conditions. Furthermore, these earlier tubercled swept-wing based studies made use of primarily tapered wings, which made isolating and understanding side-slip effects on tubercled wings more complicated. To address this, the present study focuses on the elucidation of aerodynamic performances and flow structures of a constant mean-chord tubercled wing under different combined pitch and yaw configurations, where comparisons against a baseline non-tubercled wing under similar conditions will be carried out. Steady-state numerical simulations were conducted, where lift and drag coefficients, as well as the flow behaviour and structures, under different conditions were extracted and presented later. Section 2 will describe the numerical setup, procedures and validations used, while Section 3 will see the presentation of and detailed discussions on the simulation results. Conclusions will then be provided in Section 4 to summarize the key findings from the present study.

2 Numerical setup and procedures

2.1 Tubercled and non-tubercled wing design

Figure 1a and b shows the key design characteristics of the tubercled wing studied here, where a NACA 634021 aerofoil profile is used and modified to generate a wavy leading-edge to emulate the implementation of regular tubercles. The mean chord and wing-span of both the baseline non-tubercled and tubercled wings are $c = 75$ mm and $s = 600$ mm respectively, which gives a wing aspect ratio of $s/c = 8$. The tubercle wave amplitude and wavelength used are $A/c = 0.12$ and $\lambda/c = 0.5$, where they are close to the geometries of the tubercles found in humpback whale flippers and had been studied under non-yawed conditions by [14] previously. Note that the tubercled wing described above has the same wave amplitude, wavelength and chord as one of the tubercled wings experimentally investigated by [14], as the present study seeks to extend the earlier one through numerical means. On the other hand, the present wing-span is twice that

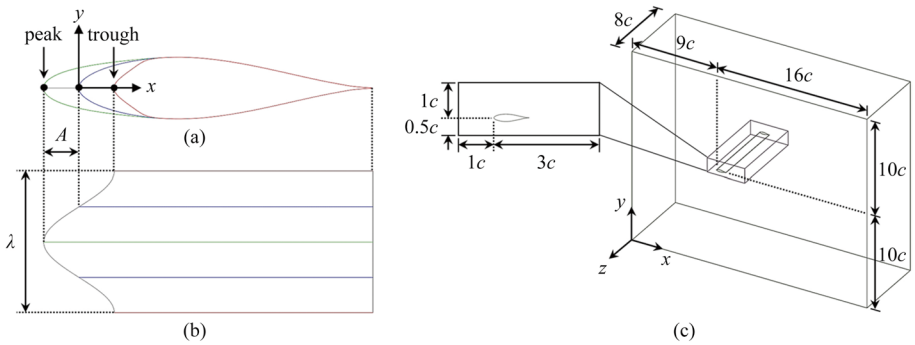

Fig. 1 **a** Side-view and **b** top-view of the tubercled wing generated by the present study. **c** shows the details of the computational domain and where the baseline and tubercled wings are located inside

used by [14] due to the need to confine any potential end-effects to the wing-tip regions to reduce any distortions to the simulation outcomes, on top of the use of appropriate boundary conditions.

Procedures adopted by [14] were also used to generate the tubercled wing for the sake of consistency, where the chords of wavy tubercled profile along the leading-edge are determined by using

$$x_{LE} = A \sin\left(\frac{2n\pi z}{s}\right), \quad 0 \le z \le s,$$

where n and z are the number of waves and location along the leading-edge. As such, there is a total of 16 tubercles along the present wing-span. To create different 2D aerofoil profiles along the wing-span that would be lofted together to produce the final 3D tubercled wing, a few conditions were set in place. Firstly, the curvature radius at the leading-edge is maintained throughout. Secondly, the maximum profile thickness location, geometry and continuity of the profile beyond the maximum thickness point are maintained as well. To accomplish that, a non-linear profile shearing transformation was used, where the abscissa of the modified cross section, x_1, and its derivative, dx_1/dx, are given as

$$x_1 = \begin{cases} x + 0.5x_{LE}\left[1 + \cos\left(\dfrac{\pi x}{0.3c}\right)\right], & 0 \le x < 0.3c, \\ x, & x \geqslant 0.3c. \end{cases}$$

$$\frac{dx_1}{dx} = \begin{cases} 1 - \dfrac{5}{3}\pi x_{LE} \sin\left(\dfrac{\pi x}{0.3c}\right), & 0 \leqslant x < 0.3c, \\ 1, & x \geqslant 0.3c. \end{cases}$$

Applying the above procedures will subsequently produce the tubercle peaks and troughs as shown in Fig. 1a and b.

2.2 Computational domain and meshing

Numerical simulations conducted in the present study are based on steady-state Reynolds-Averaged Navier-Stokes (RANS) equations approach in ANSYS Fluent^{TM}, where the Navier-Stokes equations, conservation of mass and energy equations are considered. Shear Stress Transport (SST) $k - \omega$ turbulence model was used over the standard

$k-\omega$ turbulence model, as the transport of the turbulence shear stresses can be better accounted for. While it is known that the SST $k-\omega$ turbulence model tends to over predict lift beyond the stall point due to over-estimation of boundary layer turbulence, momentum exchange and more resistant against adverse pressure gradients, results shown later will demonstrate that it does not pose significant issues here.

Figure 1c shows the cuboid computational domain used, which measures $25c \times 20c \times 8c$ in the x, y and z directions. Its size is deliberately set to be relatively large so as to avoid any potential detrimental interference from the boundaries. However, to ensure that the near-wall boundary layer and flow behaviour were captured satisfactorily by the simulations, a body of influence (see inset in Fig. 1c) described by a smaller cuboid region measuring $4c \times 1.5c \times 8c$ was used, so that a significantly higher cell density could be achieved around the test wings. Figure 2 shows the mesh configuration in general, the mesh refinements adopted around the wing surface and its trailing edge, and the surface mesh on the wing surface to improve accuracy and maintain the y^+ value to be as close to 1 as much as possible. As a result, the height of the first inflation layer has been set to 0.005 mm. Inlet velocity was set to 36 m/s, which led to a chord-based Reynolds number of $Re = 1.8 \times 10^5$, and the free stream turbulence intensity level was maintained at a nominal 0.1% of the test velocity. As the test velocity falls within the subsonic regime, the air density was kept at 1.225 kg/m^3 for all simulations. Additionally, incoming flow was set to the requisite pitch- and/or yaw-angles with the tubercled wing remaining fixed horizontally in the XZ-plane, rather than the tubercled wing geometrically pitched and/or yawed within the domain with the incoming flow remaining horizontal. Periodic boundary conditions were imposed on the sides of the domain to emulate an infinite wing, such that wing tip effects would be absent from the simulation outcomes for a better assessment of how tubercled wings are affected by non-zero yaw-angles. Finally, as mentioned earlier, to prevent any foreseen end-effects creeping into the simulation outcomes which could distort the true flow behaviour of a tubercled wing under pitching and/or yawing conditions, the doubling of the wing-span as compared to [14] should

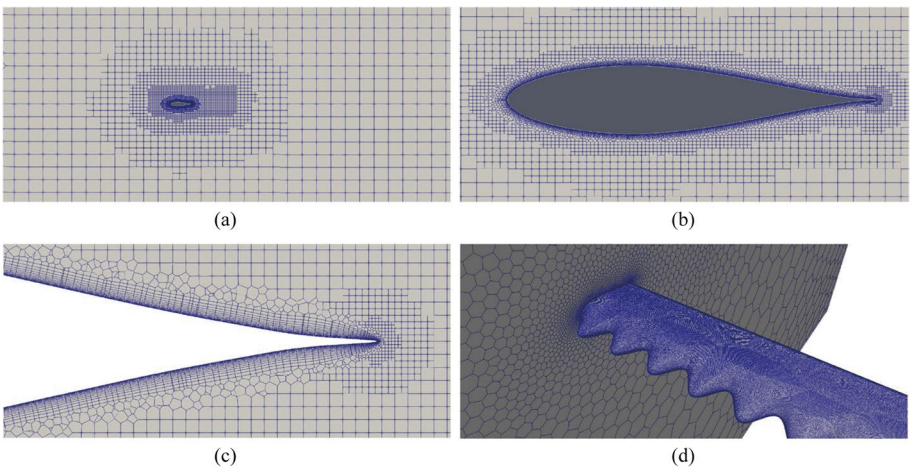

Fig. 2 **a** Cross-section of the mesh along the *XY*-plane, **b** close-up view of the mesh around the wing, **c** detail view of the mesh around the wing surface and trailing-edge and **d** surface mesh along the wing surface

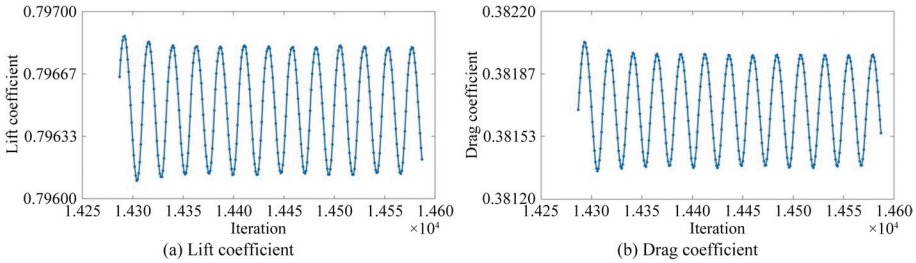

Fig. 3 Fluctuations in the **a** lift coefficient and **b** drag coefficient for the tubercled wing at $\alpha = 25°$ and $\beta = 10°$

Table 1 Details of the three mesh configurations used for mesh dependency check

Main property	Sub-category	Coarse	Medium	Fine
Local sizing	Face size mesh target (mm)	0.7	0.6	0.5
	Edge size target (mm)	0.1	0.1	0.1
	Body of influence size target (mm)	15	12	10
Inflation layer	Number of layers	20	20	20
	Transition ratio	0.4	0.4	0.4
	First cell height (mm)	0.005	0.005	0.005
General	Minimum cell length (mm)	0.7	0.1	0.1
	Maximum cell length (mm)	44.8	51.2	51.2
	Total cell count (baseline wing)	8,930,024	11,226,219	13,977,051
	Total cell count (modified wing)	9,076,370	11,411,663	14,246,725

confine the end-effects close to the wing-tips and leave flow behaviour closer to the mid-span undisturbed. Inspections of flow regions at the wing-tips at various pitch-angles of $\alpha = 6°, 18°$ and $25°$ combined with a large yaw-angle of $\beta = 30°$ showed that is indeed the case.

2.3 Mesh dependency check and experimental validation

Three different mesh configurations based on the arrangements shown in Fig. 2 were used for mesh dependency check, where the cell number increases by approximately 25% from coarse, medium to fine configurations. Convergence criterion used for the residual monitoring was relaxed at a slightly higher 10^{-5} instead of the more typical 10^{-6}, so as to ease better simulation convergences at higher pitch-angles where significant flow separations tend to occur. Nevertheless, minor force oscillations that translated into fluctuations in the lift and drag coefficients for one of the test wings as shown in Fig. 3 can be seen in the numerical outcomes. However, they remained small and careful time-averaging procedures could be used to determine reasonable mean lift and drag coefficients, which are not expected to produce a significant impact upon the conclusions of the present study. Table 1 shows the details of these three different meshes and their refinements. Steady-state RANS simulations based on SST $k - \omega$ turbulence model were subsequently conducted based on the three meshes at $\alpha = 8°$, $\beta = 0°$. This configuration was selected as the angle-of-attack is sufficiently large to introduce flow

Table 2 Grid sensitivity analysis results for baseline and modified wings for $\alpha = 8°$ and $\beta = 0°$

Wing type	Cell count	C_L	C_D	Relative C_L	Relative C_D	CGI_{C_L} (%)	CGI_{C_D} (%)
Baseline	Coarse	0.777	0.0303	1	1	0.2	0.8
	Medium	0.767	0.0302	0.987	0.996		
	Fine	0.768	0.03	0.988	0.990		
Modified	Coarse	0.4372	0.0803	1	1	1.41	0.56
	Medium	0.4067	0.0829	0.930	1.032		
	Fine	0.4164	0.0821	0.952	1.022		

separation behaviour for both the baseline and modified wings and hence, will be useful as a good mesh dependency check test case.

Table 2 shows the lift and drag coefficients of the baseline wing at $\alpha = 8°$ captured by the three different mesh types, as well as their deviations when the mesh density increases. It can be observed that using medium and fine meshes leads to relatively small changes to the lift and drag coefficients as the mesh density increases. Take for instance, the medium mesh produces deviations of 1.29% and 0.33% in the lift and drag coefficients over the coarse mesh. On the other hand, using the fine mesh produces corresponding deviations of 0.13% and 0.66% over the medium mesh. While there is an increase in the drag coefficient deviation, it remains well under 1% which is deemed to be satisfactory considering the nature of numerical simulations. What is more noteworthy is that the lift coefficient deviation has reduced to a significantly smaller 0.13% when the fine mesh is used over the medium mesh. As stall-delaying characteristics of tubercled wings are key towards their aerodynamic efficacy, emphasis is placed on as accurate as estimation of lift over drag. Reinforcing this notion are the low grid-convergence index (GCI) values [33] estimated for the lift and drag coefficients predicted by the fine mesh, which are about 0.2% and 0.8% respectively. Hence, fine mesh was used for the rest of the simulations for the baseline and tubercled wings under different pitch and yaw conditions.

To further validate the present numerical scheme, turbulence model and mesh configuration, additional simulations were carried out for the baseline wing using the fine mesh configuration under additional pitch-only conditions and compared with earlier studies by Johari et al. [34] and Dropkin et al. [35] in Fig. 4. It can be discerned that the present numerical procedures produce pre-stall lift and drag characteristics that are closer to those captured by [35]. On the other hand, predicted stall occurs at a slightly larger pitch angle of $\alpha = 19°$ as compared to [35], though post-stall lift coefficient levels are about the same. Compared to [34] however, the present stall-angle is smaller. Post-stall drag levels predicted here are also smaller than those captured by [34,35] however, though the general trend remains similar. This could be due to under-prediction of the extents of flow separations at post-stall angles, which in turn will be sensitive towards the turbulence model used. Nevertheless, Fig. 4 does demonstrate reasonable agreements between the present simulation outcomes and the past experimental results.

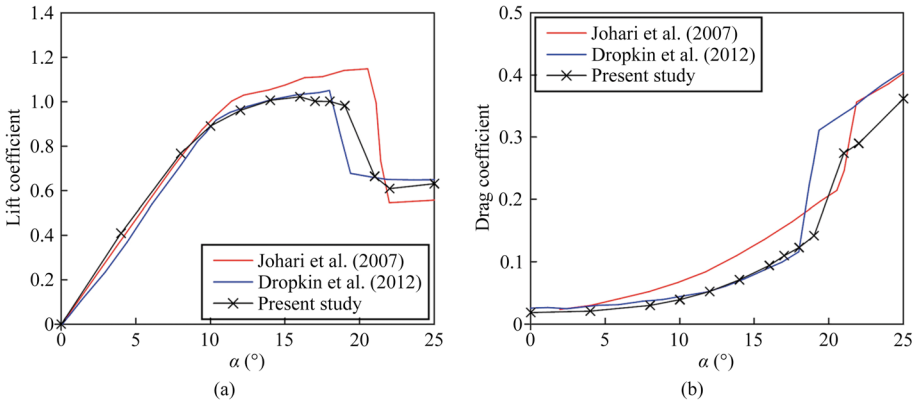

Fig. 4 Comparison of **a** lift and **b** drag curves between earlier experimental and present studies for the baseline wing under pitch-only conditions

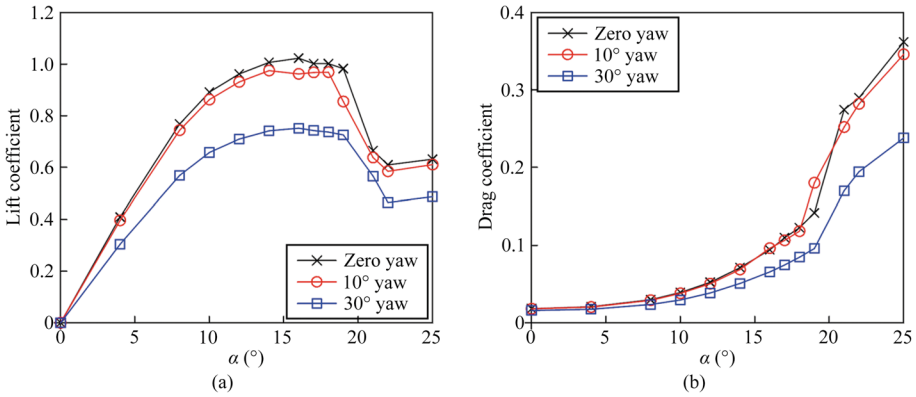

Fig. 5 Comparison of baseline wing **a** lift and **b** drag curves at zero yaw, 10° and 30° yaw configurations

3 Results and discussions

3.1 Baseline non-tubercled wing

Before going into the detailed results for the tubercled wing, it will be helpful to first establish the aerodynamic behaviour and flow structures resulting from the baseline wing subjected to yawed and non-yawed (i.e. pitched only) configurations. Figure 5 shows the lift and drag curves for the baseline wing under non-yawed, as well as $\beta = 10°$ and 30° yawed conditions, as the pitch angle varies from $\alpha = 0°$ to 25°. Results show that a small yaw angle of $\beta = 10°$ leads to minor reductions in the lift coefficients across all pitch angles as compared to the non-yawed configuration. Additionally, the stall angle has also decreased slightly to $\alpha = 18°$. As for the drag curve, slight drag reductions can be observed in post-stall conditions for $\beta = 10°$ yaw angle as compared to the non-yawed configuration, except immediately after stall has occurred. It is clear from these observations that small yaw angles do not affect the lift and drag behaviour significantly. In contrast though, the figure also shows that increasing the yaw angle to $\beta = 30°$ leads to remarkable reductions in both lift and drag coefficients across all pitch angles. Equally importantly, this indicates that the flow behaviour and flow structures at $\beta = 30°$ are expected to be quite different from those at $\beta = 10°$.

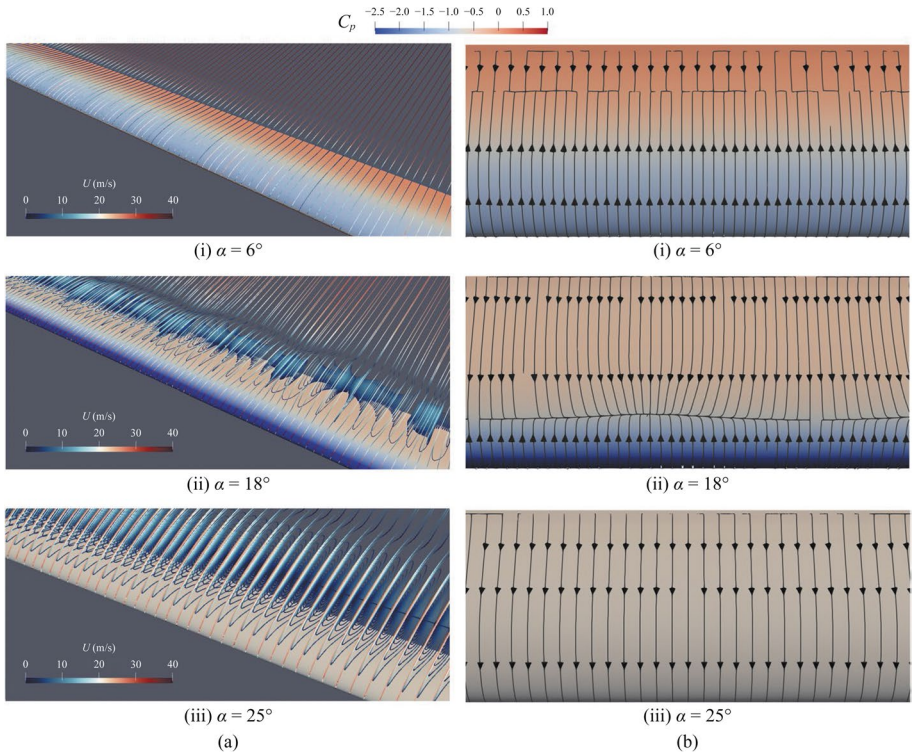

Fig. 6 Streamlines showing **a** flow separation behaviour and **b** surface streamline distributions over the baseline non-tubercled wing pitched at $\alpha = 6°, 18°$ and 25°

To investigate further on how the flow structures differ when different yaw angles are used for the baseline wing, Figs. 6, 7, and 8 show the mean streamline distributions associated with the free-stream and along the wing surfaces when it is under non-yawed and yawed conditions respectively. Note that three distinct pitch angles of $\alpha = 6°, 18°$ to 25° are considered here, as they are associated with pre-stall, just prior to stall and post-stall conditions. With reference to Fig. 6a when the baseline wing is under non-yawed conditions, the wing starts off with relatively small flow separations close to its trailing-edge at $\alpha = 6°$, before the extent of the flow separations become more significant as the pitch angle increases. This can also be discerned in Fig. 6b where the surface streamlines show the reverse flow region becomes progressively larger with the flow separation line moving upstream as the pitch angle increases. Pressure coefficient distributions along the suction surface quantify their changes as the pitch angles increases as well, where they shed light upon the lift distributions. As expected for a baseline wing without any tubercles, suction pressure coefficient increases from about $C_p = -1.5$ at $\alpha = 6°$ to in excess of $C_p = -2.5$ at $\alpha = 18°$ when it is close to the stall point. Additionally, flow separations occur at about $x/c = 0.8$ downstream of the leading-edge when pitch angle is at $\alpha = 6°$, as opposed to a much shorter approximately $x/c = 0.25$ distance downstream of the leading-edge when pitch angle is at $\alpha = 18°$. As the pitch angle continues to increase beyond the stall angle to $\alpha = 25°$ however, the suction pressure coefficient reduces drastically across the entire wing, indicating the onset of massive flow separations.

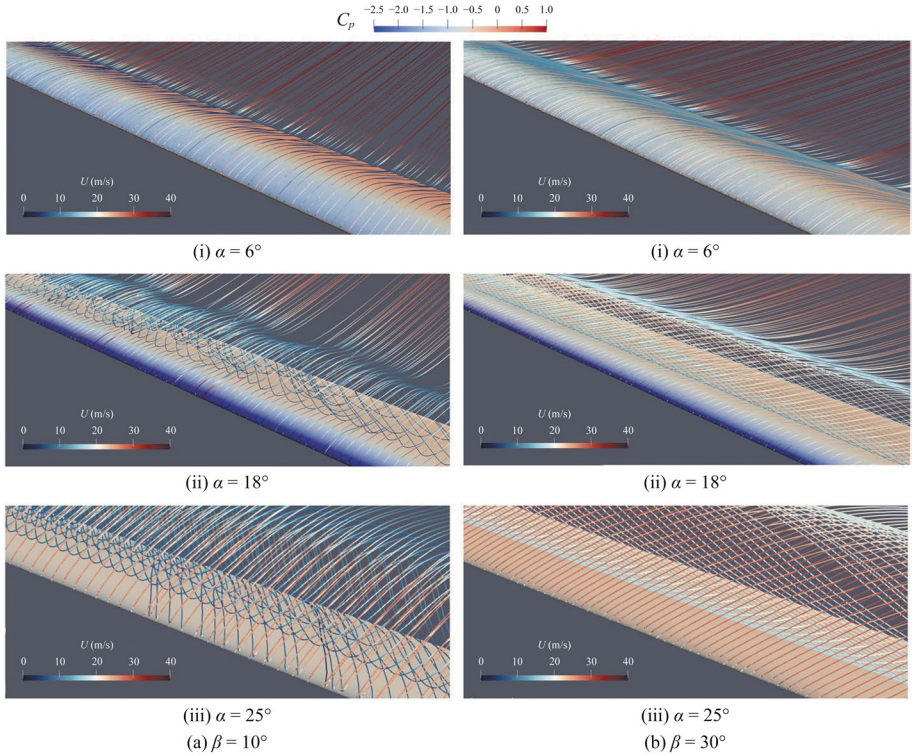

Fig. 7 Streamlines showing flow separation behaviour over the baseline non-tubercled wing under combined pitch and yaw conditions at **a** $\beta = 10°$ and **b** $\beta = 30°$, as pitch angle varies from $\alpha = 6°, 18°$ to 25°

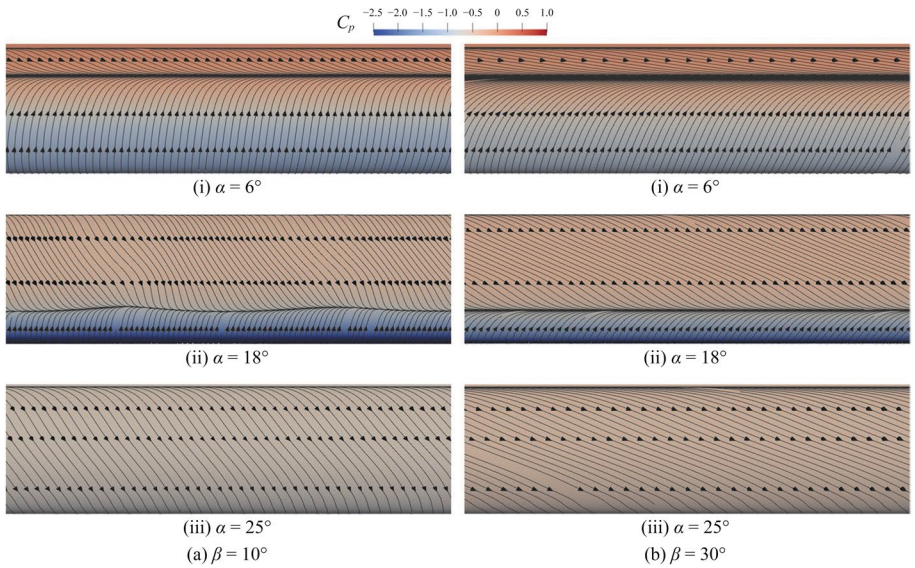

Fig. 8 Surface streamline distributions **a** flow separation behaviour and **b** surface streamline distributions under combined pitch and yaw conditions at **a** $\beta = 10°$ and **b** $\beta = 30°$, as pitch angle varies from $\alpha = 6°, 18°$ to 25°

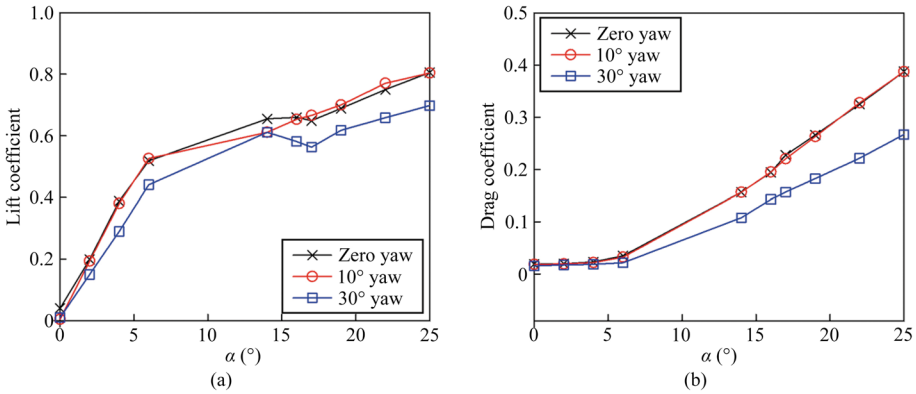

Fig. 9 Comparison of tubercled wing **a** lift and **b** drag curves at zero yaw, 10° and 30° yaw configurations

When the baseline wing is subjected to yawed conditions however, Fig. 7a shows immediate changes to the flow streamlines, particularly how they are skewed according to the yaw direction. Spanwise flows begin to manifest along the wingspan and increase correspondingly when the yaw angle goes up. This is evident in the far more highly skewed streamlines in Fig. 7b. To assess whether the introduction of non-zero yaw angles affects the flow separation extents, Fig. 8 shows the surface streamlines for the cases shown in Fig. 7. Comparing to Fig. 6b, one can discern that imposing non-zero yaw angles here do not lead to significant changes to the streamwise locations where flow separations occur. In fact, close inspection of Fig. 8a(i)-(ii) and b(i)-(ii) shows that the streamwise locations are practically similar. Interestingly though, the use of a significant $\beta = 30°$ yaw angle produces a more consistent flow separation streamwise location along the wingspan, as compared to the non-yawed and $\beta = 10°$ cases. The latter two cases produce flow separation lines that undulate along the wing spans, likely due to unstable flow behaviour just prior to abrupt stall. As for the $\beta = 10°$ case, Fig. 5a reveals that it incurs a less abrupt stall at around the same pitch angle and hence is indicative of a comparatively more stable flow behaviour prior to stall. Additionally, it is interesting to note in Fig. 8 the different streamline directions when the flows remain attached to or separated from the wing surface. As for the impact upon suction pressure coefficient distributions and flow separation lines caused by the introduction of non-zero yawed conditions, the use of $\beta = 10°$ yaw angle does not lead to significant deviations as compared to the non-yawed condition. In contrast, increasing the yaw angle to $\beta = 30°$ produces deterioration to the suction pressure levels, though flow separation points along the wing remain comparable to the smaller yaw angle. In fact, the flow separation line is more uniform for a pitch angle of $\alpha = 18°$ at $\beta = 30°$ rather than at $\beta = 10°$, as shown in Fig. 8b(ii).

3.2 Tubercled wing

Moving on to the tubercled wing, Fig. 9 shows the lift and drag curves for the tubercled wing under non-yawed, as well as $\beta = 10°$ and 30° yawed conditions, as the pitch angle varies from $\alpha = 0°$ to 25°. In terms of lift generation at zero yaw, the behaviour resembles those reported for tubercled wings in earlier studies, whereby the lift coefficient is typically lower than that for the baseline wing up till the latter's stall angle. Before

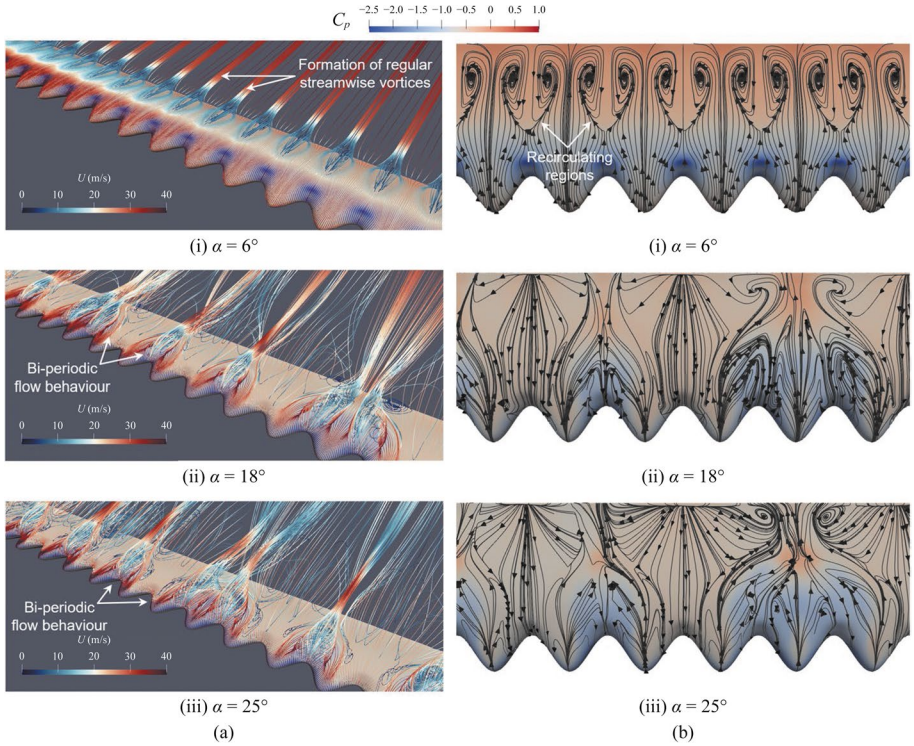

Fig. 10 Streamlines showing **a** flow separation behaviour and **b** surface streamline distributions over the tubercled wing pitched at $\alpha = 6°, 18°$ and $25°$

the stall point however, the tubercled wing continues to maintain or even under slight increments in the lift coefficient instead of incurring abrupt lift reductions. Similar to the baseline wing, an imposition of a small yaw angle of $\beta = 10°$ does not have significant effects upon the lift behaviour but increasing it to $\beta = 30°$ sees the lift coefficient to decrease across all pitch angles studied here. As for the drag coefficient, regardless of yaw angle, there are no significant drag increments at the baseline wing's stall angle, similar to what had been reported in earlier studies. However, while the use of $\beta = 10°$ confers practically no changes to the drag curve at zero yaw, increasing the yaw angle to $\beta = 30°$ leads to a significant decrease in the drag coefficient for all pitch angles used. Broadly speaking, the impact of non-zero yaw angles on baseline and tubercled wings are relatively similar.

Next, Fig. 10 shows the flow and surface streamlines associated with it under non-yawed, pitch-only conditions at the same three pitch angles as before. At a pitch angle of $\alpha = 6°$ as shown in Fig. 10a(i), the presence of the leading-edge tubercles produces very stable and regular pairs of streamwise vortices along each and every trough location close to the trailing-edge that continue to convect further far downstream of the wing. This can also be discerned in Fig. 10b(i), where the counter-rotating nature of the streamwise vortices can clearly be observed aft of every trough. Alternating low- and high-pressure regions can also be seen at the troughs and peaks respectively and indicate that velocity and pressure gradients play important roles in the formation of streamwise vortices. As the pitch angle increases to $\alpha = 18°$ and $25°$ as shown in Fig. 10a(i)-(ii), the formation of the streamwise vortices can be seen to initiate right at the troughs along the

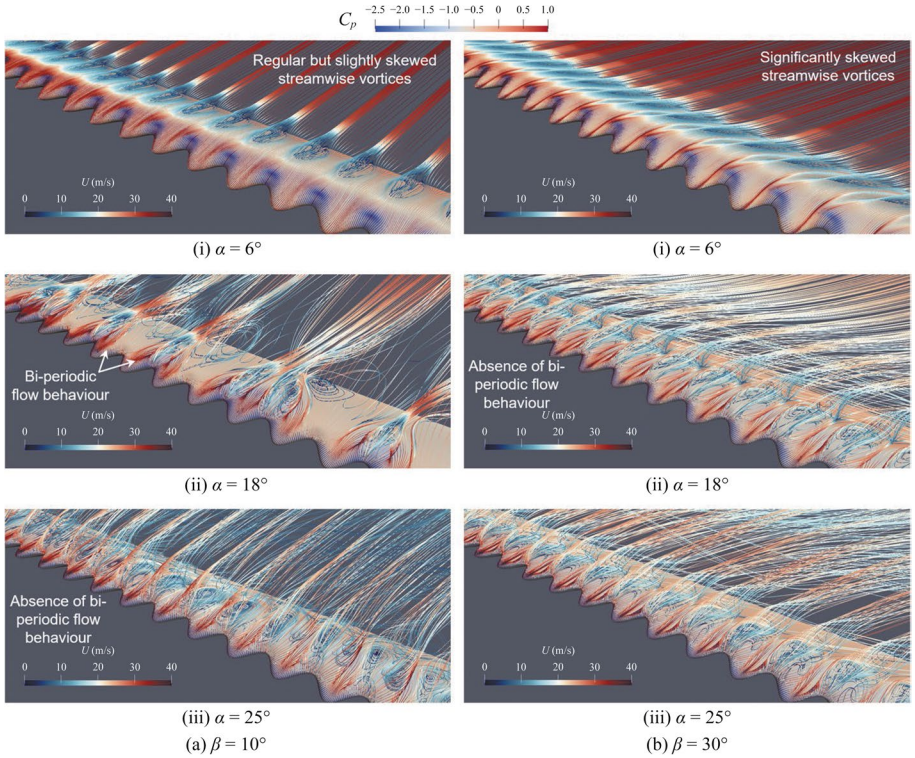

Fig. 11 Streamlines showing flow separation behaviour over the tubercled wing under combined pitch and yaw conditions at **a** $\beta = 10°$ and **b** $\beta = 30°$, as pitch angle varies from $\alpha = 6°, 18°$ to $25°$

leading-edge. What is more interesting is the observation that not all troughs will produce streamwise vortices but rather, the latter forms along roughly every other trough location though not always all the time. This can be better appreciated in Fig. 10b(ii)-(iii) where streamwise vortices could emanate from two adjacent troughs and interact mutually at near- or post-stall conditions. Such "alternating" flow behaviour in tubercled wings has been reported by [35–39] earlier and is known as a bi-periodic flow phenomenon and it typically occurs at stall and post-stall conditions, where it is postulated to result from flow interactions between adjacent troughs. Such a bi-periodic flow phenomenon would also see some form of flow compartmentalization along the tubercled wing surface, as well as a lower number of streamwise vortices along the tubercled wing surface further downstream. Subsequently, these could have an adverse impact upon the lift and drag characteristics, particularly close to the stall point as seen here. Nonetheless, successful capturing of the bi-periodic behaviour that has been reported by earlier steady-state and transient numerical studies by the present numerical simulations provides further confidence to the numerical procedures adopted here.

With the tubercled wing flow characteristics under non-yawed conditions established, Fig. 11 shows its corresponding streamline results associated with yaw angles of $\beta = 10°$ and 30°. Figure 11a(i)-(ii) shows that while the imposition of a small yaw angle of $\beta = 10°$ does not significantly affect the underlying flow behaviour at pre-stall and just prior to stall conditions (i.e., $\alpha = 6°$ and 18°), the outcome is surprisingly at post-stall condition (i.e., $\alpha = 25°$) as seen in Fig. 11a(iii). In particular, bi-periodic formations of streamwise

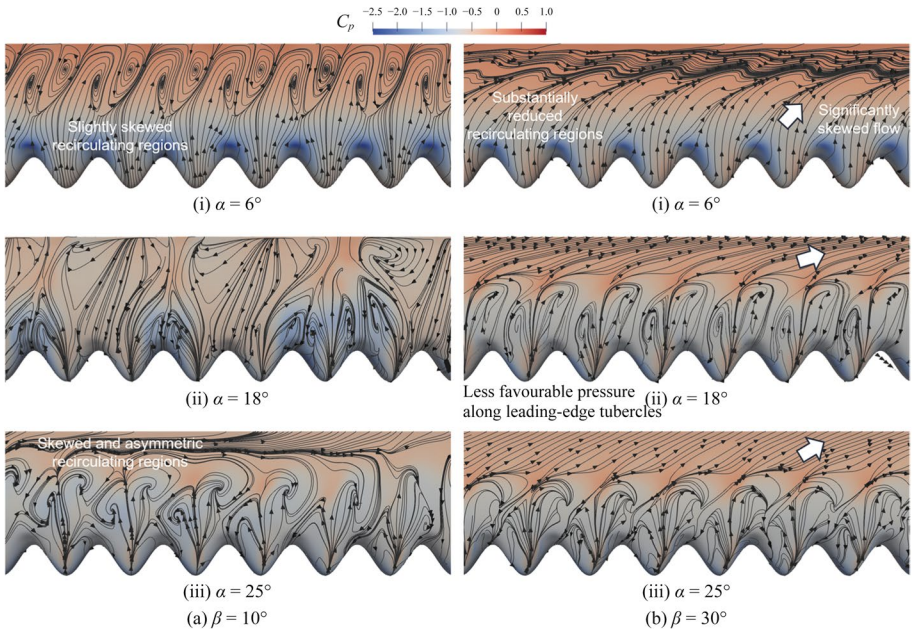

Fig. 12 Surface streamlines along the tubercled wing under combined pitch and yaw conditions at **a** $\beta = 10°$ and **b** $\beta = 30°$, as pitch angle varies from $\alpha = 6°, 18°$ to $25°$

vortices along the tubercled leading-edge as observed in Fig. 10a(iii) under pitch-only condition at $\alpha = 25°$ are now not present when a small yaw angle of $\beta = 10°$ is imposed. Closer inspection of Fig. 11a(iii) will reveal that every trough leads to the formation of a pair of streamwise vortices, reminiscent of the flow behaviour seen in Fig. 11a(i) under pre-stall condition. When a larger yaw angle of $\beta = 30°$ is used as shown in Fig. 11b(i) for $\alpha = 6°$ pitch angle, it is interesting to observe that the recirculating regions aft of every trough seen in Figs. 10a(i) and 11a(i) are weaker, indicating that moderate non-zero yaw angles are able to suppress flow separations that occur close to the tubercled wing trailing-edges. Even more interesting would be the elimination of the bi-periodic flow behaviour observed in Fig. 10a(ii) previously at this $\beta = 30°$ yaw angle when the pitch angle is $\alpha = 18°$. In this case, while flow separates from the leading-edge tubercles to form streamwise vortices aft of every trough, the recirculating regions along the leading-edge tubercles are more diminished and do not extend as much towards the trailing-edge as compared to the non-yawed and $\beta = 10°$ cases. Additionally, the now more instances of and non-bi-periodic streamwise vortices can be seen to be more skewed at this larger $\beta = 30°$ yaw angle. This behaviour extends to when the pitch angle is $\alpha = 25°$ as shown in Fig. 11b(iii), where multiple skewed streamwise vortices with more limited recirculating regions can also be observed.

The effects of imposing non-zero yaw angles upon the present tubercled wings can be further appreciated from the surface pressure and streamline results presented in Fig. 12. In agreement with the observations made in Fig. 11, the use of $\beta = 10°$ yaw angle skews the recirculating regions and streamwise vortices slightly, while using a larger $\beta = 30°$ yaw angle distorts the recirculating regions asymmetrically. This is especially the case for $\alpha = 6°$ pitch angle, where the recirculating regions close to the trailing-edge can be seen to practically disappear. At higher pitch angles of $\alpha = 18°$ and $\alpha = 25°$, the

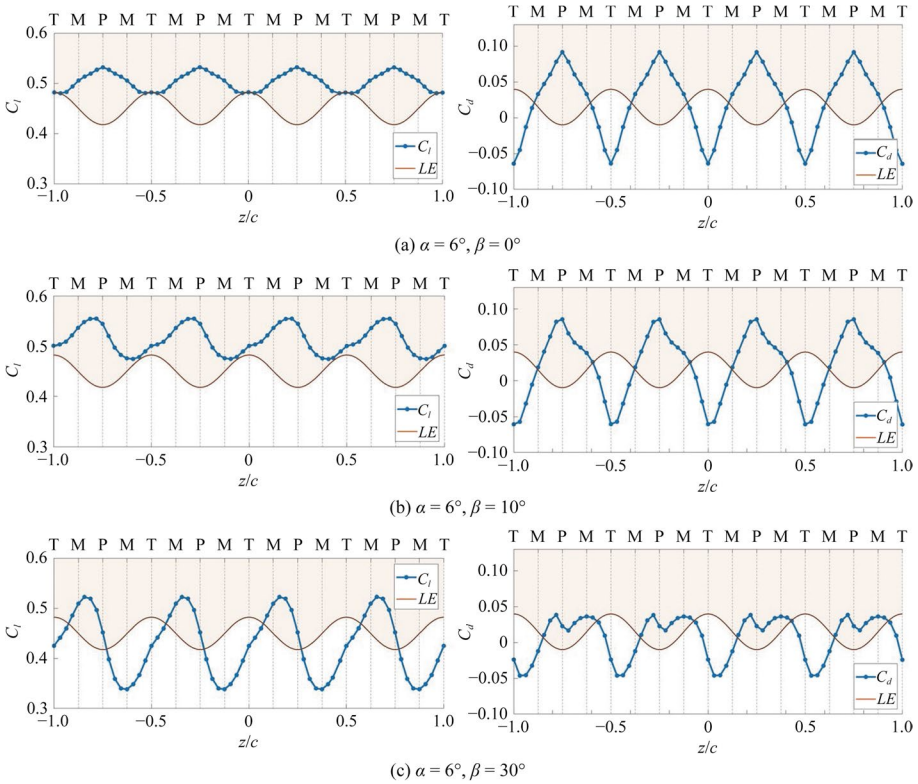

Fig. 13 Sectional lift and drag distributions over the tubercled wing at pitch angle $\alpha = 6°$ as yaw angle varies from $\beta = 0°, 10°$ to $30°$

asymmetric recirculating regions along the leading-edge tubercles give rise to lopsided counter-rotating vortices that are likely to produce unequal pressures on either side of each leading-edge tubercle. Last but not least, the low surface pressures along the leading-edge tubercles also diminish in their magnitudes, which would explain why lift generation can be seen to be adversely affected in the lift curve presented in Fig. 9a when non-zero yaw angles are imposed. Note that Fig. 9b also shows that drag levels are significantly lower when the larger $\beta = 30°$ yaw angle is used and this could be explained by lower pressure drag levels when the flow separations are more suppressed and recirculating regions more distorted.

To inspect further, a closer look at how the use of non-zero yaw angles affects the sectional lift and drag distributions along the tubercle peaks, troughs and their mid-planes will now be had. Similar to the previous section, the impact of the two different yaw angles at three distinct pitch angles of $\alpha = 6°, 18°$ and $25°$ will be investigated. Figure 13a shows the result for pitch angle $\alpha = 6°$ only, where the zero yaw-angle scenario leads to repeating sinusoidal-like high and low sectional lift and drag coefficient distributions along the peak and trough locations respectively. In this case, minimum and maximum lift coefficients are approximately 0.48 and 0.53 respectively, while minimum and maximum drag coefficients are about -0.07 to 0.1 respectively. This is within expectations as Fig. 10a(i)-(ii) has that while the troughs produce lower pressure coefficients at the leading-edge, subsequent flow separations and recirculating regions produced along the

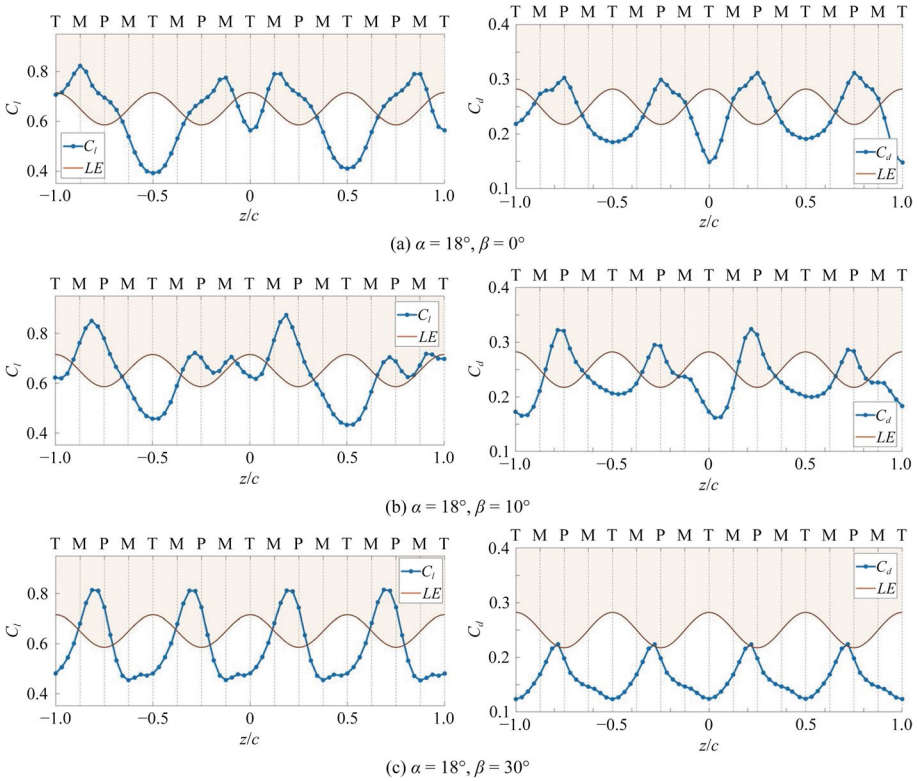

Fig. 14 Sectional lift and drag distributions over the tubercled wing at pitch angle $\alpha = 18°$ as yaw angle varies from $\beta = 0°, 10°$ to $30°$

trough locations close to the trailing-edge mean that the sectional lift coefficient along the troughs will remain lower than that along the peak locations. When a yaw angle of $\beta = 10°$ is imposed upon the same tubercled wing however, as shown in Fig. 13b, two interesting changes can be observed immediately. Firstly, the magnitudes of the maximum and minimum sectional lift coefficients (i.e., about 0.48 and 0.56 respectively now) increase with larger discrepancies between them and secondly, maximum and minimum sectional lift locations are now skewed due to the yaw angle. The same is also true for the drag coefficient distribution where it is now skewed due to the yaw angle, though the minimum and maximum levels remain relatively similar to the non-yawed case. Increasing the yaw angle to $\beta = 30°$ only serves to accentuate the discrepancy between the maximum and minimum sectional lift coefficients as shown in Fig. 13c, with a range of about 0.33 to 0.52. In contrast, the opposite is true for the drag coefficient, where the minimum and maximum drag coefficients are approximately -0.05 and 0.04.

As for larger pitch angles of $\alpha = 18°$ shown in Fig. 14, the sectional lift and drag coefficients show more irregular variations along the wingspan up to $\beta = 10°$ yaw angle. Collating with results shown in Figs. 10 and 12 earlier, these non-sinusoidal variations are due to the skewed counter-rotating vortices aft of the leading-edge tubercles. In fact, they appear to be manifestations of the bi-periodic structures observed previously, where multiple peaks and troughs of different amplitudes and wavelengths are combined. On the other hand, increasing the yaw angle to $\beta = 30°$ returns its variation back to a more sinusoidal-like distribution, as shown in Fig. 14c. It should be noted that the minimum

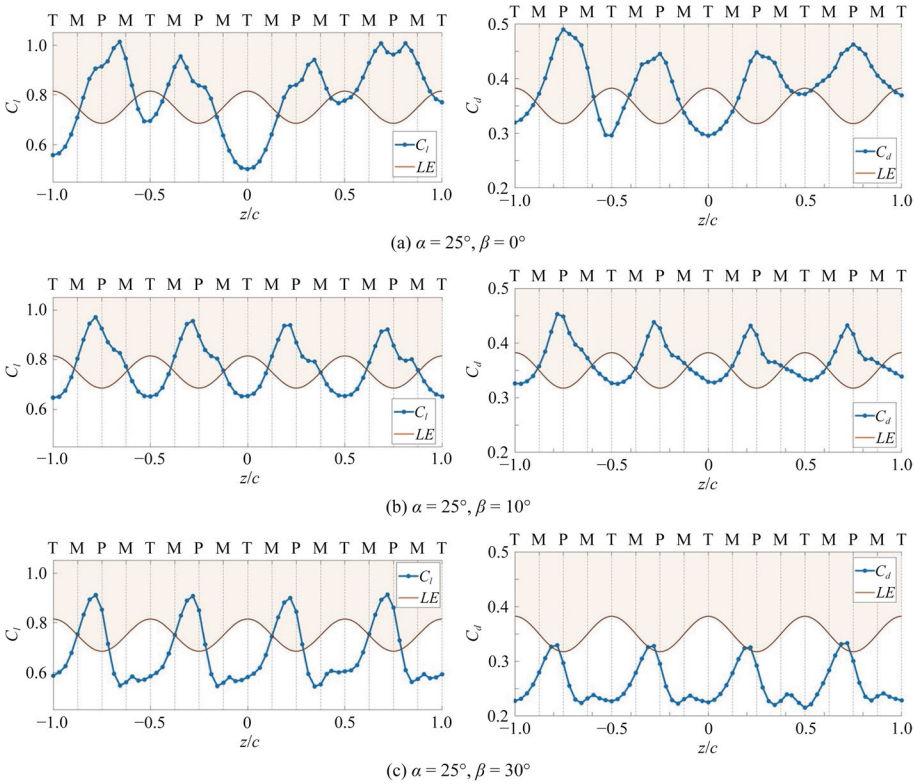

Fig. 15 Sectional lift and drag distributions over the tubercled wing at pitch angle $\alpha = 25°$ as yaw angle varies from $\beta = 0°, 10°$ to $30°$

and maximum lift coefficients do not differ much, typically between 0.4 to 0.8 across all yaw angles. While this is true for the drag coefficients for $\beta = 0°$ and $10°$ at around 0.15 to 0.31, those for $\beta = 30°$ show a narrower range of between 0.12 to 0.23. As for the largest pitch angle of $\alpha = 25°$ shown in Fig. 15, only the zero-yaw case demonstrates a less regular sectional lift and drag coefficient variations, with those at $\beta = 10°$ and $30°$ yaw angles showing more sinusoidal-like distributions. Collating with Fig. 11, the irregular sectional lift and drag coefficients are again due to the bi-periodic flow behaviour where adjacent recirculating regions along the leading-edge tubercles pair up. The minimum and maximum lift coefficients are around 0.55 and 1.0, while those for the drag coefficients are about 0.3 to 0.5. More intriguingly, using non-zero yaw angles here suppress the said bi-periodic flow behaviour where larger yaw angles become more effective in doing so. It is worthwhile to mention that the bi-periodic flow behaviour occurs naturally and is difficult to predict due to its non-linearity. Nevertheless, the minimum and maximum lift coefficients are approximately 0.65 and 1, while the corresponding values for the drag coefficients are around 0.33 to 0.45, for $\beta = 10°$ test case. As the yaw angle increases to $\beta = 30°$, the maximum lift coefficient reduces to about 0.9 with little change to the minimum lift coefficient, while the drag coefficient ranges between 0.21 to 0.33.

From the sectional lift and drag coefficient results, it can be seen that their distributions and range support earlier lift/drag curves, whereby both lift and drag tend to decrease as the yaw angle increases to $\beta = 30°$. On the other hand however, earlier

results also indicate that non-zero yaw angles suppress or reduce the extent of bi-periodic behaviour. Hence, the present findings suggest a rather interesting notion that using a significant non-zero yaw angle flow configuration could prove to be beneficial in terms of more predictable and potentially more stable flow behaviour, so long the reduction in lift performance is acceptable. In practical terms, this could mean that tubercled wings are less sensitive towards adverse cross-wind effects and remain functional even when the cross-wind angle is substantial. Having said that, future experimental studies are planned to validate the present findings, particularly through the use of surface oil flow visualizations [40] and particle image velocimetry measurements [41, 42].

4 Conclusions

Results from a steady-state numerical study conducted on a tubercled wing immersed in free-stream with non-zero yaw angles of $\beta = 10°$ and 30° show that, firstly, it does not incur abrupt reductions in lift performance at the stall angle associated with the baseline wing, thus similar to the situation under zero-yaw configurations. Secondly, the imposition of an increasingly larger yaw angle on the free-stream leads to increasing suppression of the flow separations and recirculating regions along the leading-edge tubercles, thus producing less advantageous pressure coefficient levels. Thirdly, increasingly larger free-stream yaw angle reduces the occurrences of bi-periodic flow behaviour for the streamwise vortices and is seen as improving the flow stability and controllability of tubercled wing aerodynamic characteristics. Impacts of different yaw angles upon the overall lift and drag performances, flow behaviour and vortex structures, as well as sectional lift variations have been also clarified, with their mutual relationships better understood.

Acknowledgements
The authors acknowledge the support for the research project by ETH Zurich and Nanyang Technological University, Singapore.

Authors' contributions
T. H. New: Conceptualization (Lead); Supervision (Lead); Investigation (Equal); Writing - original draft (Lead); Writing - review and editing (Equal). S. Mandrà: Investigation (Equal); Visualization (Lead); Writing - review and editing (Equal).

Funding
Not applicable.

Availability of data and materials
Data is available upon reasonable request to the corresponding author.

Declarations

Competing interests
The authors have no conflicts of interest to declare.

Received: 22 January 2024 Accepted: 17 May 2024
Published online: 05 September 2024

References

1. New TH, Chan YX, Koh GC et al (2014) Effects of corrugated aerofoil surface features on flow-separation control. AIAA J 52:206–211
2. Izquierdo DOD, Marques FD (2021) Experimental analysis of passive bio-inspired covert feathers for stall and post-stall performance enhancement. Meccanica 56:2671–2689
3. Liu K, Song B, Xue D et al (2022) Numerical study of the aerodynamic effects of bio-inspired leading-edge serrations on a heaving wing at a low Reynolds number. Aerosp Sci Technol 124:107529

4. Othman AK, Zekry DA, Saro-Cortes V et al (2023) Aerial and aquatic biological and bioinspired flow control strategies. Comms Eng 2:30
5. Fang Z, Gong C, Revell A et al (2019) Passive separation control of a NACA0012 airfoil via a flexible flap. Phys Fluids 31:101904
6. Piquee J, López Canalejo I, Breitsamter C et al (2019) Aerodynamic analysis of a generic wing featuring an elasto-flexible lifting surface. Adv Aerodyn 1:20
7. Nath DS, Pujari PC, Jain A et al (2019) Drag reduction by application of aerodynamic devices in a race car. Adv Aerodyn 3:4
8. Smith TA, Klettner CA (2022) Airfoil trailing-edge noise and drag reduction at a moderate Reynolds number using wavy geometries. Phys Fluids 34:117107
9. Arif I, Lam GCY, Wu D et al (2020) Passive airfoil tonal noise reduction by localized flow-induced vibration of an elastic panel. Aerosp Sci Technol 107:106319
10. Mayer YD, Zang B, Azarpeyvand M (2020) Aeroacoustic investigation of an oscillating airfoil in the pre- and post-stall regime. Aerosp Sci Technol 103:105880
11. Ji X, Wang L, Ravi S et al (2023) Aerodynamic and aeroacoustic performance of a pitching foil with trailing edge serrations at a high Reynolds number. Theor Comput Fluid Dyn (ahead of print). https://doi.org/10.1007/s00162-023-00677-8
12. Miklosovic DS, Murray MM, Howle LE et al (2004) Leading-edge tubercles delay stall on humpback whale (Megaptera novaeangliae) flippers. Phys Fluids 16:L39–L42
13. Hansen KL, Kelso RM, Dally BB (2011) Performance variations of leading-edge tubercles for distinct airfoil profiles. AIAA J 49:185–194
14. Wei Z, New TH, Cui YD (2015) An experimental study on flow separation control of hydrofoils with leading-edge tubercles at low Reynolds number. Ocean Eng 108:336–349
15. Wei Z, Zang B, New TH et al (2016) A proper orthogonal decomposition study on the unsteady flow behaviour of a hydrofoil with leading-edge tubercles. Ocean Eng 121:356–368
16. Wei Z, New TH, Cui YD (2016) Surface flow topology visualizations of wings with leading-edge tubercles under pitch, yaw and roll conditions. In: 17th international symposium on flow visualization, Gatlinburg, 19–22 June 2016
17. Wei Z, New TH, Cui YD (2018) Aerodynamic performance and surface flow structures of leading-edge tubercled tapered swept-back wings. AIAA J 56:423–431
18. Wei Z, New TH, Lian L et al (2019) Leading-edge tubercles delay flow separation for a tapered swept-back wing at very low Reynolds number. Ocean Eng 181:173–184
19. Ng BF, New TH, Palacios R (2016) Effects of leading-edge tubercles on wing flutter speeds. Bioinspir Biomim 11:036003
20. Sudhakar S, Karthikeyan N, Venkatakrishnan L (2017) Influence of leading edge tubercles on aerodynamic characteristics of a high aspect-ratio UAV. Aerosp Sci Technol 69:281–289
21. Huang X (2019) A theoretical study of serrated leading edges in aerofoil and vortical gust interaction noise. Adv Aerodyn 1:6
22. Cai C, Zhou T, Liu S et al (2022) Modeling of the compartmentalization effect induced by leading-edge tubercles. Phys Fluids 34:087104
23. Weber PW, Howle LE, Murray MM (2010) Lift, drag, and cavitation onset on rudders with leading-edge tubercles. Mar Technol SNAME N 47:27–36
24. Shormann DE, In Het Panhuis M (2020) Performance evaluation of humpback whale-inspired shortboard surfing fins based on ocean wave fieldwork. PLoS One 15(4):e0232035
25. Butt FR, Talha T (2019) Numerical investigation of the effect of leading-edge tubercles on propeller performance. J Aircr 56:1014–1028
26. Stark C, Shi W, Atlar M (2021) A numerical investigation into the influence of bio-inspired leading-edge tubercles on the hydrodynamic performance of a benchmark ducted propeller. Ocean Eng 237:109593
27. Sun S, Zhi Y, Li X et al (2022) Numerical investigation on cavitating wake dynamic of a propeller with bionic tubercle leading-edge. Ocean Eng 252:111240
28. Keerthi MC, Rajeshwaran MS, Kushari A et al (2016) Effect of leading-edge tubercles on compressor cascade performance. AIAA J 54:912–923
29. Shi W, Atlar M, Norman R et al (2016) Numerical optimization and experimental validation for a tidal turbine blade with leading-edge tubercles. Renew Energy 96:42–55
30. Ke W, Hashem I, Zhang W et al (2022) Influence of leading-edge tubercles on the aerodynamic performance of a horizontal-axis wind turbine: A numerical study. Energy 239:122186
31. Fish FE, Battle JM (1995) Hydrodynamic design of the humpback whale flipper. J Morphol 225:51–60
32. New DTH, Ng BF (2020) Flow control through bio-inspired leading-edge tubercles. Springer Nature Switzerland AG, Cham
33. Celik IB, Ghia U, Roache PJ et al (2008) Procedure for estimation and reporting of uncertainty due to discretization in CFD applications. J Fluids Eng 130:078001
34. Johari H, Henoch C, Custodio D et al (2007) Effects of leading-edge protuberances on airfoil performance. AIAA J 45:2634–2642
35. Dropkin A, Custodio D, Henoch CW et al (2012) Computation of flow field around an airfoil with leading-edge protuberances. J Aircr 49:1345–1355
36. Malipeddi AK, Mahmoudnejad N, Hoffmann KA (2012) Numerical analysis of effects of leading-edge protuberances on aircraft wing performance. J Aircr 49:1336–1344
37. Câmara JFD, Sousa JMM (2013) Numerical study on the use of a sinusoidal leading edge for passive stall control at low Reynolds number. In: 51st AIAA aerospace sciences meeting including the new horizons forum and aerospace exposition, Grapevine, 7–10 January 2013
38. Rostamzadeh N, Hansen KL, Kelso RM et al (2014) The formation mechanism and impact of streamwise vortices on NACA 0021 airfoil's performance with undulating leading edge modification. Phys Fluids 26:107101

39. Cai C, Zuo Z, Maeda T et al (2017) Periodic and aperiodic flow patterns around an airfoil with leading-edge protuberances. Phys Fluids 29:115110
40. Cheawchan A, Mohamed MA, Ng BF et al (2022) A numerical investigation on flow past skewed vortex generators ahead of a backward facing ramp. Aerosp Sci Technol 123:107435
41. Zang B, New TH (2017) Near-field dynamics of parallel twin jets in cross-flow. Phys Fluids 29:035103
42. Soria J, New TH, Lim TT et al (2003) Multigrid CCDPIV measurements of accelerated flow past an airfoil at an angle of attack of 30°. Exp Therm Fluid Sci 27:667–676

Publisher's Note